J Am Oil Chem Soc (2008) 85:961–972
DOI 10.1007/s11746-008-1279-x

ORIGINAL PAPER

Crystallization Behavior of Fatty Acid Methyl Esters

Robert O. Dunn

Received: 8 April 2008 / Revised: 13 June 2008 / Accepted: 15 July 2008 / Published online: 9 August 2008

Abstract Biodiesel from most agricultural feedstocks has flow properties that are prone to startup and operability problems during cold weather. Biodiesel from soybean oil is generally a mixture of long-chain fatty acid alkyl esters composed of 0.15–0.20 mass fraction saturated esters (melting point [MP] $\gg$ 0 °C) mixed with unsaturated esters (MP $<$ 0 °C). This work investigates the crystallization properties of two saturated fatty acid methyl esters (FAME) commonly found in biodiesel from soybean oil. Differential scanning calorimetry (DSC) heating and cooling scans of methyl palmitate (MeC16), methyl stearate (MeC18) and methyl oleate (MeC18:1) in pure form were analyzed. Crystallization behavior in ternary FAME mixtures was inferred by the application of thermodynamic models based on ideal solution and freezing-point depression theories. Activity coefficients for MeC16 and MeC18 in MeC18:1 solvent were determined by analyzing DSC cooling curves for binary FAME mixtures. Eutectic points were predicted by both models. Crystallization onset temperatures inferred from freezing point depression theory were more accurate than those for ideal solutions with respect to a direct DSC cooling curve analysis of corresponding ternary mixtures. This work shows that the crystallization onset temperature (cloud point) of biodiesel may be predicted by freezing-point depression theory if the activity coefficients of the component FAME are known.

Keywords Activity coefficient · Biodiesel · Cloud point · Cold flow properties · Crystallization onset temperature · Differential scanning calorimetry · Enthalpy of fusion · Freezing point depression · Melting point · Saturated · Unsaturated

Abbreviations

CP	Cloud point of diesel fuels (°C or K)
DSC	Differential scanning calorimeter
FAME	Fatty acid methyl ester(s)
FP	Freezing point onset temperature of pure component (°C or K)
MeC16	Palmitic acid methyl ester
MeC18	Stearic acid methyl ester
MeC18:1	Oleic acid methyl ester
MP	Melting point onset temperature of pure component (°C or K)
SD	Standard deviation of mean value

List of symbols

C_p, C_p^L, C_p^S	heat capacity of pure component (kJ/mol-K); "L" = liquid, "S" = solid
ΔC_p	differential heat capacity $[C_p^L - C_p^S]$ (kJ/mol-K)
g_S	osmotic coefficient of solvent (calculated from Eq. 2)
g_S^H	osmotic coefficient of solvent calculated assuming $\Delta C_p = 0$
ΔH_{fus}	enthalpy of fusion (kJ/mol)

The use of trade, firm, or corporation names in this publication is for the information and convenience of the reader. Such use does not constitute an official endorsement or approval by USDA or ARS of any product or service to the exclusion of others that may be suitable.

R. O. Dunn (✉)
Food and Industrial Oils Research,
United States Department of Agriculture (USDA),
Agricultural Research Service (ARS),
National Center for Agricultural Utilization Research,
Peoria, IL, USA
e-mail: robert.dunn@ars.usda.gov

ΔH_m	enthalpy of melting (kJ/mol)
P_H	temperature of minimum heat flow of melting peak on DSC curve (°C)
P_F	temperature of maximum heat flow of freezing peak on DSC curve (°C)
R_g	gas constant = 8.3144 J/mol K
T	temperature (°C or K)
T_f	crystallization onset temperature of FAME mixture (°C or K)
$T_f^{[1]}, T_f^{[2]}$	T_f calculated from Eq. 1 or 2 (°C or K)
T_f^{DSC}	crystallization onset temperature of ternary FAME mixture measured by DSC (°C or K)
x, x_i	mole fraction of species "i" in a mixture; $i = 1$ for MeC16, 2 for MeC18, S for MeC18:1
y, y_i	mass fraction of species "i" in a mixture (g/g); $i = 1$ for MeC16, 2 for MeC18
δT_f	absolute deviation between T_f values calculated from theory and measured directly from DSC cooling curves $[\lvert\{T_f^{[1]}$ or $T_f^{[2]}\} - T_f^{DSC}\rvert]$ (°C or K)
γ, γ_i	activity coefficient of species "i" in liquid phase, calculated from Eq. 2; $i = 1$ for MeC16, 2 for MeC18
γ_i^H	activity coefficient of species "i" in liquid phase, calculated from Eq. 2 assuming $\Delta C_p = 0$; $i = 1$ for MeC16, 2 for MeC18

Introduction

Biodiesel, derived from the transesterification of vegetable oils or animal fats with a simple alcohol, has many fuel properties and other characteristics that make it an attractive alternative diesel fuel or extender. The most common forms of biodiesel in the United States are fatty acid methyl esters (FAME) of lipids such as soybean oil, rapeseed oil, canola oil, used cooking oil, waste greases or tallow. Applications for biodiesel include diesel-powered transportation trucks, automobiles and farm vehicles, locomotives, aircraft, stationary power generators, boilers and heaters.

Biodiesel is renewable, environmentally innocuous due to its low toxicity and ability to rapidly biodegrade, and has a high flash point, making it relatively safe to store and handle. Its gross heat of combustion, specific gravity and kinematic viscosity are comparable to those of conventional diesel. Biodiesel blends well in conventional diesel fuel, enhancing cetane number, which may decrease ignition delay time [1–4]. Biodiesel in very small blend ratios (≤2 vol%) restores lubricity and antiwear characteristics in low-sulfur conventional diesel that are lost during hydrotreatment to remove sulfur [3, 5]. Life cycle analysis of biodiesel indicates that it returns three times the energy required to produce it and has a net negative carbon dioxide balance [6]. According to a comprehensive review conducted by the US Environmental Protection Agency [7], when blended with conventional fuel, biodiesel significantly reduces hydrocarbons, carbon monoxide, and particulate matter in exhaust emissions. Although nitrogen oxide emissions increase slightly, this increase is generally <5% for blend ratios up to 20 vol%. Biodiesel is also reported to reduce smoke opacity, sulfur dioxide and polycyclic aromatic hydrocarbons in emissions [1–3].

Despite its many virtues, the cold flow properties of biodiesel will affect its performance in moderate climates during cold weather. There is evidence that soybean oil biodiesel raises performance issues as ambient temperatures approach 0–2 °C. As overnight temperatures fall into this range, high-melting point (MP) saturated FAME in biodiesel nucleate and form crystals in the fuel. As the crystals grow they restrict or block flow through fuel lines and filters during startup the following morning, possibly leading to fuel starvation and engine failure [8]. Findings from a recent report [9] urged that biodiesel should be stored at temperatures (T) ≥ 6 °C above its cloud point (CP) before splash blending with conventional diesel.

The relative concentration of saturated and unsaturated FAME species in biodiesel may have a significant effect on the thermodynamics of nucleation and crystallization during cold weather. Biodiesel derived from palm oil or tallow has a relatively high saturated fatty acid content, leading to CP values in the range 13–17 °C [10–12]. Similarly, biodiesel derived from used cooking oil or waste grease has very poor cold flow properties [11, 13].

Dry fractionation (winterization) of biodiesel from soybean oil significantly improves cold flow properties [14–16]. This approach was effective because it decreased the total concentration of saturated FAME from 16–20 to <6 wt%. Saturated FAME in biodiesel from soybean oil are mostly composed of methyl palmitate (MeC16) and stearate (MeC18). These FAME have high MP (≥30 °C), while the remaining unsaturated FAME present (typically methyl oleate [MeC18:1], linoleate and linolenate) have MP ≤ −19 °C [17, 18]. Earlier studies [14, 19] showed that dry fractionation of biodiesel from soybean oil can reduce the CP to −20 °C, the pour point to −21 °C, the cold filter plugging point to −19 °C, and the low-temperature flow test to −16 °C.

Increasing our understanding of how fatty acid composition affects the crystallization properties of FAME is essential if we are to improve the cold flow properties of biodiesel. One approach that accounts for the impacts of the individual components of a solution is the application of freezing point depression theory to FAME mixtures.

Holder and Winkler [20] observed freezing point depression behavior in dewaxed gas oil spiked with pairs of long-chain (C_{20}–C_{28}) *n*-alkanes with total concentrations of 2, 4 and 8 wt%. They compared the results with CP data and determined that the mixtures follow qualitative trends from freezing-point depression theory for independent crystallization where each species solidifies in its pure form. Analysis of crystallized solids showed that the C_{20}/C_{22} *n*-alkane pair formed a solid solution where the solid phase consists of mixed species. Increasing the difference in molecular weight (chain length) of the *n*-alkane pairs increased the preference for independent crystallization over solid solution. This study concluded that freezing point depression theory accurately predicted the cold flow behavior of model fuel mixtures by following the crystallization behavior of a binary system in a solvent that did not freeze at the temperatures studied. Finally, the theory was employed to explain how a small quantity of heavy wax can influence the cold flow properties of mixtures.

Toro-Vazquez et al. [21] applied freezing-point depression theory to interpret nonisothermal differential scanning calorimetry (DSC) heating and cooling scan data for binary mixtures of tripalmitin and palm stearin in sesame seed oil solvent. This work employed a form of the Hildebrand equation for ideal solutions:

$$\ln(x) = -\frac{\Delta H_{\text{fus}}}{R_{\text{g}}}\left[\frac{1}{T_{\text{f}}} - \frac{1}{MP}\right] \tag{1}$$

where x = solute mole fraction, ΔH_{fus} = enthalpy of fusion of the pure solute, R_{g} = gas constant, T_{f} = crystallization onset temperature of the solute in solution, and MP = melting point of the solute in pure form. Equation 1 fits quite well to results for palm stearin/sesame seed oil mixtures, while tripalmitin/sesame seed oil mixtures with less than 0.98% tripalmitin deviated from ideality.

Suppes et al. [22] critiqued a number of theoretical and empirical models developed for application to mixtures composed of *n*-alkanes, olefins and other hydrocarbons. They concluded that freezing-point depression theory was the only fundamentally correct method for modeling crystallization processes in organic liquid mixtures. They developed two models based on how the solid phase develops: independent crystallization, where each species solidifies in its pure form; and solid solution, where the solid phase consists of varying compositions of all species cocrystallizing from liquid phase. This study successfully applied both models to predict the freezing behavior and cold flow properties of Fischer–Tropsch fuels.

The form of the model developed by Suppes et al. [22] that applies to the independent crystallization of solid precipitates is described in the following equation:

$$\ln(\gamma_i x_i) = -\frac{\Delta H_{\text{fus}}}{R_{\text{g}}}\left[\frac{MP - T_{\text{f}}}{MP(T_{\text{f}})}\right] - \frac{\Delta C_{\text{p}}}{R_{\text{g}}}\left[1 - \frac{MP}{T_{\text{f}}} + \ln\left(\frac{MP}{T_{\text{f}}}\right)\right] \tag{2}$$

where γ_i and x_i are the activity coefficient and mole fraction of species "*i*" in the liquid phase, ΔH_{fus}, MP and T_{f} are parameters for species "*i*" as defined in Eq. 1, and ΔC_{p} is the differential heat capacity of species "*i*" between the liquid and solid phases, $(C_{\text{p}}^{\text{L}} - C_{\text{p}}^{\text{S}})$. The activity coefficient (γ_i) in Eq. 2 accounts for nonideal behavior in the liquid phase, while the second term on the right hand side corrects for variation in ΔH_{fus} with respect to temperature.

Imahara et al. [23] employed the freezing-point depression theory model to characterize CP behavior of biodiesel and investigate effects of fatty acid composition in long-chain (C_{16}–C_{18}) FAME mixtures. They reduced Eq. 2 to a form resembling Eq. 1 by setting $\gamma_i = 1$ due low ambient pressures and assuming that ΔC_{p} in the second term was negligible. Acquiring $\Delta H_{\text{fus}} = \Delta H_{\text{m}}$ (enthalpy of melting) from literature and MP data of pure FAME from an automatic CP analyzer, they calculated T_{f} data for various multicomponent FAME mixtures. Upon comparing calculated results with T_{f} data obtained directly from the CP analyzer, binary FAME mixtures showed good agreement with calculated T_{f} data. Deviations between calculated and measured T_{f} data were $\leq$5 °C for mixtures composed of up to five FAME. This work also showed that T_{f} was essentially independent of the composition of unsaturated FAME present in the solvent phase of the mixture.

The development of a thermodynamic model for predicting CP behavior in FAME mixtures is of huge importance to fuel producers, suppliers and terminal operators, who must deal with biodiesel during cold weather. The present work meets this challenge by investigating the application of equations based on ideal solution and freezing-point depression theory to mixtures composed of saturated and unsaturated long-chain FAME mixtures. Subambient DSC was employed to measure ΔH_{fus}, MP and ΔC_{p} of pure MeC16 and MeC18, and to measure T_{f} of binary mixtures in MeC18:1 solvent. Both models (Eq. 1 and 2) were evaluated to calculate T_{f} values for ternary mixtures composed of both saturated FAME in MeC18:1 solvent. Calculated results were compared with T_{f} data inferred from the analysis of DSC cooling curves.

Experimental Procedures

Materials

Pure MeC16 (99+ wt% methyl hexadecanoate), MeC18 (99+% methyl octadecanoate) and MeC18:1 (99+% methyl-(9Z)-octadecenoate) were obtained from Nu Chek Prep (Elysian, MN, USA). Sample purity was confirmed by gas chromatography/mass spectrometry (GC/MS) analysis. Indium and sapphire (aluminum oxide) crystals for calibrating the DSC were supplied by TA Instruments (New Castle, DE, USA).

GC/MS

Verification of FAME purity was performed on a Agilent Technologies (Palo Alto, CA, USA) model 6890 GC equipped with an HP-5MS capillary column (30 m × 0.25 mm ID, 0.5 μm film) and coupled with a model 5973N mass selective detector operating in ionization mode at 70 eV. All mathematical analyses were performed on a desktop personal computer using a standard spreadsheet application.

DSC Scans

Subambient DSC analyses were conducted using a Q1000 DSC instrument system from TA Instruments (New Castle, DE, USA). The instrument system consisted of the following: (1) a DSC measurement cell and module; (2) a refrigerated cooling system for scans conducted in subambient temperature ranges; and (3) a model 5000 PC-based controller for conducting experimental runs and analyzing the resulting scans. An autosampler built into the instrument module was programmed to place reference and sample pans in precise positions within the measurement cell. Sample purge gas was dry nitrogen with a flow rate of 50.00 ml/min regulated by a mass flow controller.

The theory behind DSC is the measurement of heat flow through a sample by comparing its heat flow inside a sample pan with that measured simultaneously for an empty but otherwise identical reference pan. Standard aluminum pans were employed for sample and reference pans for calibration runs, while hermetically sealed type aluminum pans were used for the analysis of pure and mixed FAME. Samples were carefully weighed before sealing in either type of pan. The autosampler was used to place sample and reference pans for all analyses conducted in the present study.

DSC Calibrations

Four types of calibrations were necessary to prepare the Q1000 DSC cell in order to conduct the present study. The first type was a baseline calibration, designated by the instrument manufacturer as the T_{zero}^{TM} calibration. This calibration required two experiments, the first running without samples or pans and the second running with two large (~95 mg) sapphire disks placed on both sample and reference positions in the cell. Both experiments were run with the following program: (1) equilibrate at $T = 400$ °C; (2) hold isothermally for 5 min; (3) equilibrate at $T = -90$ °C; (4) hold isothermally for 5 min; (5) ramp at 20 °C/min to $T = 400$ °C; (6) hold isothermally for 5 min; (7) ramp at 20 °C/min to $T = -90$ °C; (8) hold isothermally for 5 min; and (9) equilibrate at $T = 50$ °C. Results from the two calibration experiments were employed by instrument control software to automatically account for sensor thermal capacitance and resistance values and to normalize for baseline effects during scans.

The second and third types of calibration, cell constant (enthalpy) and temperature correction, were conducted using the same sample data file. These calibrations were performed by heating an indium reference standard through its melting transition and comparing MP and ΔH_m values calculated from the data file with theoretical values (156.79 °C and 28.66 J/g; data supplied by TA Instruments). Cell constant and temperature correction factors were calculated and set automatically by the instrument control software. The cell constant is the ratio between measured and theoretical ΔH_m values; the temperature correction is the difference between measured and theoretical MP.

The fourth type of calibration was for heat capacity (C_p). This calibration was only performed for the analysis of C_p on pure FAME. For this calibration, a small sapphire crystal was weighed and sealed in a sample pan and scanned by the following program: (1) equilibrate at $T_1 = 60$ °C; (2) hold isothermally for 5 min; and (3) cool at 5 °C/min to $T_2 = -80$ °C. Once the scan was complete, the results were plotted as C_p versus T to determine the measured C_p at a T close to an average between the T_1 and T_2 (−13.15 °C). The measured C_p (0.7754 J/g °C) was divided into the theoretical C_p of sapphire at the same T (0.6846 J/g °C; data supplied by TA Instruments). Once the resultant C_p factor (0.8829) was manually entered into the instrument control software application, subsequent scans could be plotted in terms of absolute C_p versus T curves.

DSC Analyses

Heating (melting) curve DSC scans for pure FAME were conducted with the following generalized program: (1) equilibrate at $T = T_1$; (2) hold isothermally at T_1 for 10 min; (3) ramp at 10 °C/min to $T = T_2$; (3) hold isothermally at T_2 for 30 min; (4) ramp at 5 °C/min back to T_1. For MeC16, MeC18 and MeC18:1, $T_2 = 10$, 20 and

−45 °C and T_1 = 50, 60 and 40 °C. Each heating scan was analyzed to determine the melting onset temperature (MP), the maximum peak temperature (P_H) and the enthalpy of melting (ΔH_m) data. Mean values and standard deviations (SD) for each of these parameters were inferred from an analysis of replicate heating scans conducted on three individual samples.

Cooling (freezing) curve DSC scans for pure, binary and ternary FAME mixtures were conducted according to the following program: (1) equilibrate at T_1; (2) ramp at 5 °C/min to $T = T_2$; (3) hold isothermally at T_2 for 1 min; and (4) ramp at 5 °C/min back to T_1. For pure MeC16, MeC18 and MeC18:1, T_1 = 50, 60 and 40 °C and T_2 = −10, −5 and −65 °C, and each cooling scan was analyzed to determine the crystallization onset temperature (FP), the maximum peak temperature (P_F) and the enthalpy of fusion (ΔH_{fus}) data. For binary and ternary mixtures, T_1 = 40 °C and T_2 =−60 °C, and each scan was analyzed to determine the crystallization onset temperature of the mixture (T_f) plus P_F and ΔH_{fus}. Mean values and SDs for all parameters were inferred from an analysis of replicate cooling scans conducted on three individual samples.

Cooling curves for pure FAME were also conducted to analyze for absolute C_p in the liquid and solid phases (C_p^L and C_p^S). Once calibrated as explained above, these scans were conducted between T_1 = 60 °C and T_2 = −10 °C for MeC16 and MeC18 and between T_1 = 40 °C and T_2 = −70 °C for MeC18:1. Each cooling scan was plotted as C_p versus T and analyzed utilizing the model 5000 controller to report C_p data at selected T. For example, C_p^L of MeC16 was taken at T = 40 °C, while C_p^S of MeC16 was taken at T = 5 °C. Replicate scans were performed three times on each FAME (same sample), and the results were interpreted to yield C_p^L and C_p^S values, as summarized in Table 1.

Results and Discussion

Analysis of Pure FAME

DSC heating (melting) and cooling curves for pure MeC16, MeC18 and MeC18:1 samples are shown in Figs. 1 and 2,

Table 1 Heat capacities of pure FAME in liquid and solid phases

FAME	Liquid phase		Solid phase	
	T (°C)	C_p^L(J/mol-K)	T (°C)	C_p^S(J/mol-K)
MeC16	40.00	640 ± 7.1	5.00	535 ± 8.6
MeC18	50.00	634.6 ± 0.86	15.00	539 ± 4.4
MeC18:1	−30.00	410 ± 13	−65.00	320 ± 12

FAME fatty acid methyl esters, *MeC16* methyl palmitate, *MeC18* methyl stearate, *MeC18:1* methyl oleate, T, measurement temperature, C_p^L, C_p^S, heat capacities in the liquid and solid phase

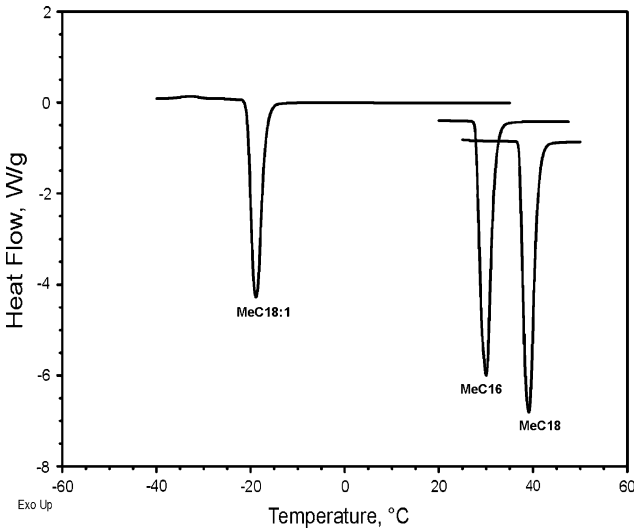

Fig. 1 Differential scanning calorimetry (DSC) heating curves for pure fatty acid methyl esters (FAME). Curve offsets on the y-axis: −0.4630 W/g for MeC16; −0.9259 W/g for MeC18. Legend: MeC18:1 = methyl oleate; MeC16 = methyl palmitate; MeC18 = methyl stearate

respectively. Each FAME yielded melting and freezing peaks featuring very sharp onset temperatures. Onset temperatures (that is, MP and FP) were determined by extrapolating a line tangent to the inflection point (sharpest decrease or increase) on the lead edge of the peak. P_H values were taken as the temperature of minimum heat flow in melting peaks (Fig. 1), while P_F values were taken as the temperature of maximum heat flow in freezing peaks (Fig. 2). ΔH_m and ΔH_{fus} values were obtained by integrating the peaks in the corresponding heat flow versus temperature curves.

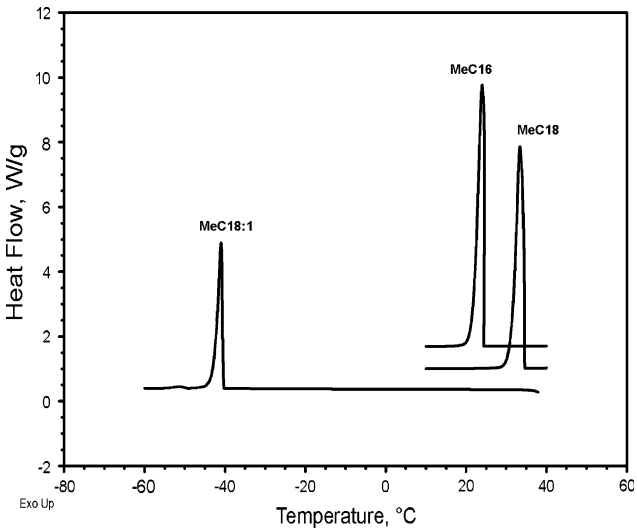

Fig. 2 DSC cooling curves for pure FAME. Curve offsets on the y-axis: +0.4748 W/g for MeC18:1; +1.7424 W/g for MeC16; +1.0328 W/g for MeC18. See Fig. 1 for abbreviations

Analysis of the heating scans in Fig. 1 yielded MP = 27.78 °C, P_H = 30.03 °C and ΔH_m = 49.90 kJ/mol for MeC16; MP = 37.06 °C, P_H = 39.10 °C and ΔH_m = 57.04 kJ/mol for MeC18; and MP = −20.73 °C, P_H = −18.90 °C and ΔH_m = 41.80 kJ/mol for MeC18:1. Similar analysis of the scans in Fig. 2 yielded FP = 24.72 °C, P_F = 23.98 °C and ΔH_{fus} = 49.46 kJ/mol for MeC16; FP = 34.57 °C, P_F = 33.38 °C and ΔH_{fus} = 55.37 kJ/mol for MeC18; and FP = −40.48 °C, P_F = −40.96 °C and ΔH_{fus} = 24.46 kJ/mol for MeC18:1.

A summary of the results from DSC heating and cooling scans on three replicate pure FAME samples is presented in Table 2. In general, the results from heating scans were very accurate (within SDs < 0.5 °C for MP and P_H and SDs < 1 kJ/mol for ΔH_m). Although results from cooling scans showed SDs < 1 °C for FP and P_F, ΔH_{fus} results yielded SDs that were 11–13% relative to mean values.

The results in Table 2 compared well with data reported in the literature. MP values of 30 and 32–34 °C were reported for MeC16, and values of 38 and 39 °C were reported for MeC18 [17, 18]. MP = −19.9 °C was also reported for MeC18:1 [18]. Imahara et al. [23] measured CP = 28 °C for pure MeC16, 37 °C for pure MeC18 and −14 °C for pure MeC18:1, and employed these as MP data in their model calculations. FP results in Table 2 were noticeably lower than MP data. Results for saturated FAME in the present study were in good agreement with Rodrigues Jr. et al. [24], who reported FP = 23.2 °C for MeC16 and 31.6 °C for MeC18.

Very little data on ΔH_{fus} or ΔH_m of pure FAME are available in the literature. Imahara et al. [23] reported ΔH_m = 55.35 and 62.34 kJ/mol for MeC16 and MeC18, respectively. They also substituted the ΔH_m of oleic acid (39.60 kJ/mol) for that of MeC18:1 in their work. Continuing the comparison with data for fatty acids, ΔH_m data in the literature show some variability, such as values from 42.04 to 54.28 kJ/mol for palmitic acid and from 56.59 to 62.47 kJ/mol for stearic acid [17, 18, 25].

Table 2 Results from DSC analyses of pure FAME

FAME	MP (°C)	P_H (°C)	ΔH_m (kJ/mol)
(a) Heating curves at 5 °C/min			
MeC16	27.79 ± 0.042	29.9 ± 0.31	49.4 ± 0.53
MeC18	37.05 ± 0.050	39.0 ± 0.17	56.5 ± 0.77
MeC18:1	−20.71 ± 0.059	−18.9 ± 0.14	40.9 ± 0.98
FAME	FP (°C)	P_F (°C)	ΔH_{fus} (kJ/mol)
(b) Cooling curves at 5 °C/min			
MeC16	24.4 ± 0.93	23.7 ± 0.80	47 ± 5.0
MeC18	33.7 ± 0.79	32.7 ± 0.58	51 ± 6.5
MeC18:1	−40.6 ± 0.29	−41.1 ± 0.16	28 ± 3.1

DSC, differential scanning calorimetry; *MP*, melting point (melting peak onset) temperature of pure compound; P_H, melting peak minimum temperature (exothermic); ΔH_m, enthalpy of melting; *FP*, freezing point (crystallization peak onset) of pure compound; P_F, freezing peak maximum temperature (exothermic); ΔH_{fus}, enthalpy of fusion. See Table 1 for other abbreviations

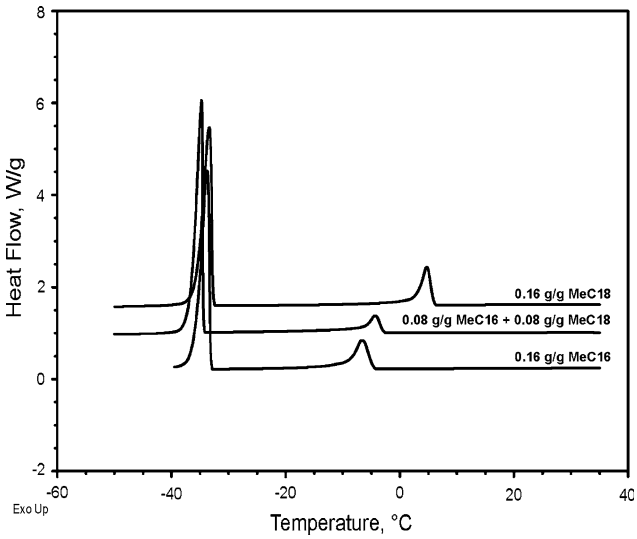

Fig. 3 DSC cooling curves for binary and ternary FAME mixtures. Curve offsets on the *y*-axis: +1.4136 W/g for 0.16 g/g MeC18; +0.8377 W/g for 0.08 g/g MeC16 +0.08 g/g MeC18. See Fig. 1 for abbreviations

Analysis of Binary FAME Mixtures

DSC cooling curves for two binary mixtures consisting of 0.16 mass fraction (g/g) MeC16 and MeC18 in MeC18:1 solvent are shown in Fig. 3. For comparison, the DSC cooling curve for a ternary FAME mixture with 0.08 g/g MeC16 and 0.08 g/g MeC18 is also shown. Each curve exhibits two distinct peaks, one solvent peak at T_f = −34.52 to −32.78 °C and one solute peak at T_f = −4.73 °C for the MeC16 binary mixture, +5.90 °C for the MeC18 binary mixture, and −2.94 °C for the ternary mixture. A summary of the results from replicate DSC cooling scans for two series of binary FAME mixtures, one each with MeC16 and MeC18 as solute, is shown in Table 3.

Comparing data in Tables 2 and 3, T_f values of MeC16 and MeC18 in binary mixtures with MeC18:1 occur at temperatures far below the MP of either solute in pure form. This observation suggested that solute freezing point depression is occurring in FAME mixtures. The expression shown in Eq. 1 indicates that a plot of ln(*x*) versus T_f^{-1} results in a straight line with slope = $-(\Delta H_{fus}/R_g)$ and intercept = MP^{-1}. Thus, for ideal solutions the slope and intercept inferred from the application of least squares linear regression may be employed to calculate ΔH_{fus} and MP of the pure solute if T_f is known for a series of *x*.

Table 3 Results from DSC analyses of binary FAME mixtures in MeC18:1 solvent

y_i	Solute = MeC16			Solute = MeC18		
	x_1	T_f {MeC16} (°C)	T_f {MeC18:1} (°C)	x_2	T_f {MeC18} (°C)	T_f {MeC18:1} (°C)
0.04	0.044	−29.4[a]	−33.00 ± 0.042	0.040	−12.3 ± 0.40	−32.34 ± 0.053
0.08	0.087	−18.3 ± 0.98	−33.13 ± 0.021	0.080	−2.2 ± 0.27	−32.47 ± 0.050
0.12	0.13	−12 ± 1.0	−33.23 ± 0.055	0.12	2 ± 1.3	−32.56 ± 0.010
0.16	0.17	−4.8 ± 0.26	−33.23 ± 0.021	0.16	6.2 ± 0.81	−32.7 ± 0.11
0.20	0.22	−1.8 ± 0.40	−33.33 ± 0.015	0.20	10.7 ± 0.85	−32.82 ± 0.050

Cooling curves at 5 °C/min

y_i, mass fraction of solute in binary mixture with MeC18:1, x_1, mole fraction of MeC16 in MeC18:1, x_2, mole fraction of MeC18 in MeC18:1, T_f, crystallization onset temperature of freezing peaks in FAME mixtures. See Table 1 for other abbreviations

[a] Only one of three replicate cooling scans demonstrated a separate peak for MeC16

Analysis of the data in Table 3 for MeC16 solute resulted in a straight line with an adjusted correlation factor (R^2) = 0.994, leading to calculated ΔH_{fus} = 31.3 kJ/mol and MP = 32.1 °C for pure MeC16. Comparing with corresponding results in Table 2 indicates that the crystallization of MeC16 in MeC18:1 solvent may behave nonideally. Similar analysis of the data for MeC18 solute also resulted in a straight line with R^2 = 0.994, leading to calculated ΔH_{fus} = 44.5 kJ/mol and MP = 37.0 °C for pure MeC18. While the calculated ΔH_{fus} was slightly less than its measured value shown in Table 2, the calculated MP of pure MeC18 agreed quite well with its measured value (37.05 ± 0.050 °C).

Solute Activity Coefficients

Equation 2 was applied to data from the analysis of pure FAME and binary mixtures in MeC18:1 solvent (Tables 1, 2 and 3) to calculate γ_1 for a series of x_1 for MeC16 and γ_2 for a series of x_2 for MeC18. Results are summarized in Table 4.

For both saturated FAME solutes, $\gamma_i < 1$, indicating that interactions between solute and MeC18:1 molecules in the binary mixtures were different from interactions between solute molecules in pure form. Since $\gamma_i < 1$ and the activity of component "i" (a_i) = $\gamma_i \cdot x_i$, then $a_i < x_i$ for both solutes in MeC18:1 solvent, indicating that the free energy of mixing either MeC16 or MeC18 in binary solution with MeC18:1 was likely less than the free energy of mixing for the corresponding ideal solution. Moreover, at near-constant x_i, $\gamma_1 < \gamma_2$, because the molecular structure of MeC18 more closely resembles that of MeC18:1 than MeC16.

Table 4 Activity coefficients from the DSC analysis of binary FAME mixtures in MeC18:1 solvent

Solute = MeC16			Solute = MeC18		
x_1	γ_1	γ_1^H	x_2	γ_2	γ_2^H
0.044	0.3911	0.2890	0.040	0.7293	0.6070
0.087	0.4756	0.3951	0.080	0.8132	0.7283
0.13	0.5031	0.4392	0.12	0.7547	0.6930
0.17	0.6566	0.6022	0.16	0.7650	0.7166
0.22	0.6557	0.6113	0.20	0.8465	0.8078

γ_i, activity coefficient of solute species "i" in the liquid phase, calculated from Eq. 2; γ_i^H, activity coefficient of solute species "i" calculated from Eq. 2, assuming $(C_p^L - C_p^S) = 0$. See Tables 1, 2 and 3 for other abbreviations

Sensitivity analysis of the γ_i data in Table 4 was performed by calculating the variances caused by deviations in the experimental parameters ΔH_{fus}, MP, T_f, and ΔC_p. For each parameter, upper and lower limits for γ_i were calculated using Eq. 2 by substituting its mean value ± SD (see Table 2) while keeping all remaining parameters constant. Varying ΔH_{fus} by its SD caused significant deviations in γ_i for both MeC16 (−0.1433 for x_1 = 0.0870; +0.2316 for x_1 = 0.0437) and MeC18 (−0.2767 to +0.4458 for x_2 = 0.0397). For both MeC16 and MeC18, overestimating ΔH_{fus} values by +SD caused smaller deviations in γ_i than underestimating by −SD. Furthermore, substituting ΔH_m for ΔH_{fus} in Eq. 2 decreases γ_1 by ≤0.0903 for MeC16 and γ_2 by ≤0.2500 for MeC18. This analysis suggests that great care must be taken to acquire accurate ΔH_{fus} values for each solute species in solution.

Sensitivity analysis of the remaining three parameters showed very little absolute deviation relative to the corresponding ±SD values for either MeC16 (<0.002 for MP; <0.04 for T_f; < 0.015 for ΔC_p) or MeC18 (<0.03 for MP; <0.08 for T_f; <0.007 for ΔC_p). The aforementioned report by Imahara et al. [23] suggested that the contribution of the ΔC_p term to the overall value of the right-hand side of Eq. 2 is negligible because $\Delta C_p \sim 0$. For the present study, the γ_i^H values shown in Table 4 represent results from Eq. 2 obtained by assuming this was the case. These results show that γ_i^H were significantly lower than γ_i for both MeC16 (6.7–23.8%) and MeC18 (4.6–16.8%).

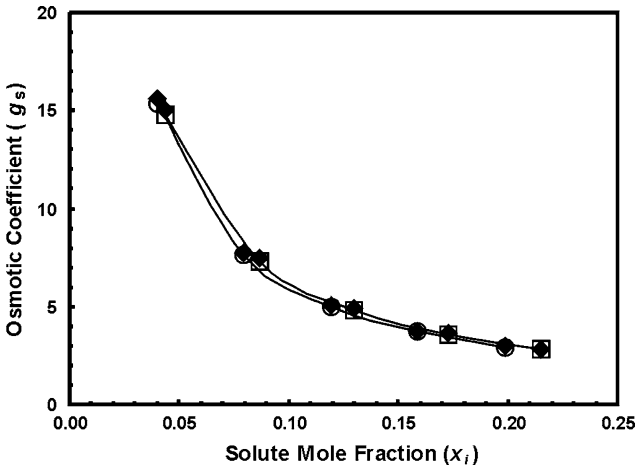

Fig. 4 Osmotic coefficient (g_S) of solvent (MeC18:1) calculated from Eq. 3. Legend: *open squares*, binary mixtures with MeC16; *circles*, binary mixtures with MeC18; *filled diamonds*, values calculated from the application of Eq. 3 assuming $\Delta C_p = (C_p^L - C_P^S) = 0$. C_p^L, C_P^S = Heat capacities of pure solute in liquid (L) and solid (S) forms. See Fig. 1 for other abbreviations

Solvent Osmotic Coefficients

It was convenient to calculate the osmotic coefficient (g_S) of MeC18:1 solvent as a function of solvent mole fraction (x_S) by the following equation:

$$g_s[\ln(x_s)] = -\frac{\Delta H_{fus}}{R_g}\left[\frac{MP - T_f}{MP(T_f)}\right] - \frac{\Delta C_p}{R_g}\left[1 - \frac{MP}{T_f} + \ln\left(\frac{MP}{T_f}\right)\right] \quad (3)$$

where the parameters ΔH_{fus}, MP, and ΔC_p are measured for pure solvent and T_f represents the onset of crystallization of the solvent peak from a binary FAME mixture (see Tables 1 and 2). Results from the calculation of g_S for MeC18:1 as a function of x_i (solute mole fraction) for binary mixtures with MeC16 and MeC18 are shown in Fig. 4.

The two superimposed curves show a relatively small deviation in g_S between mixtures with the two different solutes, suggesting that the crystallization thermodynamics of MeC18:1 solvent were not greatly affected by the selection of MeC16 or MeC18 solutes. Also plotted in Fig. 4 are data points representing "g_S^H" values calculated from Eq. 3 assuming $\Delta C_p = 0$ (analogous to γ_i^H of solutes). Results for corresponding solutes show very little deviation between g_S and g_S^H values, suggesting that the contribution of ΔC_p to the calculation of g_S was negligible for MeC18:1.

Both curves in Fig. 4 show that g_S decreases with increasing solute mole fraction (x_i), suggesting that they approach a constant value as x_i exceeds 0.20. Overall, results in Fig. 4 show that FAME mixtures demonstrate nonideal behavior, especially at low solute concentrations.

Predicting T_f of Ternary FAME Mixtures

Following the accurate measurement of ΔH_{fus}, MP and ΔC_p, the calculation of T_f values for ternary FAME mixtures using ideal solution or freezing-point depression theory models was straightforward. Essentially, both models predict that each solute species crystallizes independently with respect to the presence, concentration or activity of the other solute species at low temperatures. Thus, either Eq. 1 or 2 is applied to calculate T_f values for each solute species present in a ternary FAME mixture, where the predicted T_f value of the solution is taken from the greater of the two values.

For ideal solutions, this process was conducted by rearranging Eq. 1 and directly calculating T_f. For freezing-point depression theory, a less direct method was necessary. First, for mixtures with known concentrations of solute species (x_i), γ_i values were interpolated based on the results in Table 4. Second, a trial-and-error process was applied to mixtures with known x_i by estimating a T_f value for species "i," plugging it into Eq. 2, calculating γ_I, and comparing with the corresponding interpolated γ_I value. If the calculated and interpolated γ_I values were equivalent, then T_f of species "i" was the estimated value. Otherwise, the trial-and-error step is repeated with a new T_f value. Once T_f values were obtained independently for given concentrations of MeC16 and MeC18 in ternary mixtures, the predicted T_f value of the mixture was taken as the greater of these two calculated values.

Results for ideal FAME mixtures with a constant total solute mass fraction $(y_1 + y_2) = 0.16$ g/g are shown in Fig. 5a. Taking the highest calculated T_f value at all solute compositions, the predicted ternary mixture curve exhibited a minimum $T_f = 269.75$ K near $x_1 = 0.12$ for MeC16. This eutectic point corresponds to a ternary composition where the MeC16/MeC18 mole ratio $(x_1/x_2) = 2.2$. Thus, T_f of ternary mixtures is controlled by the crystallization behavior of MeC18 for compositions where $x_1 < 0.12$ and by MeC16 for compositions where $x_1 > 0.12$. Imahara et al. [23] reported comparable behavior for ideal binary mixtures of MeC16 and MeC18, with a eutectic point at nearly the same $x_1/x_2 = 2.3$.

Results from the calculation of T_f values for nonideal FAME ternary mixtures are shown in Fig. 5b for the application of Eq. 2 and in Fig. 5c for Eq. 2, assuming $\Delta C_p = 0$ and $\gamma_i = \gamma_i^H$. Analogous to ideal solutions, the calculated T_f curve from Eq. 2 in Fig. 5b exhibited a minimum $T_f = 261.45$ K, though this eutectic point occurred at higher $x_1 = 0.13$ for MeC16, which corresponded to a composition with $x_1/x_2 = 3.1$. Furthermore, the calculated T_f curve in Fig. 5c demonstrated near-identical behavior to the curve in Fig. 5b, where minimum $T_f = 261.47$ K, $x_1 = 0.13$ and $x_1/x_2 = 3.2$.

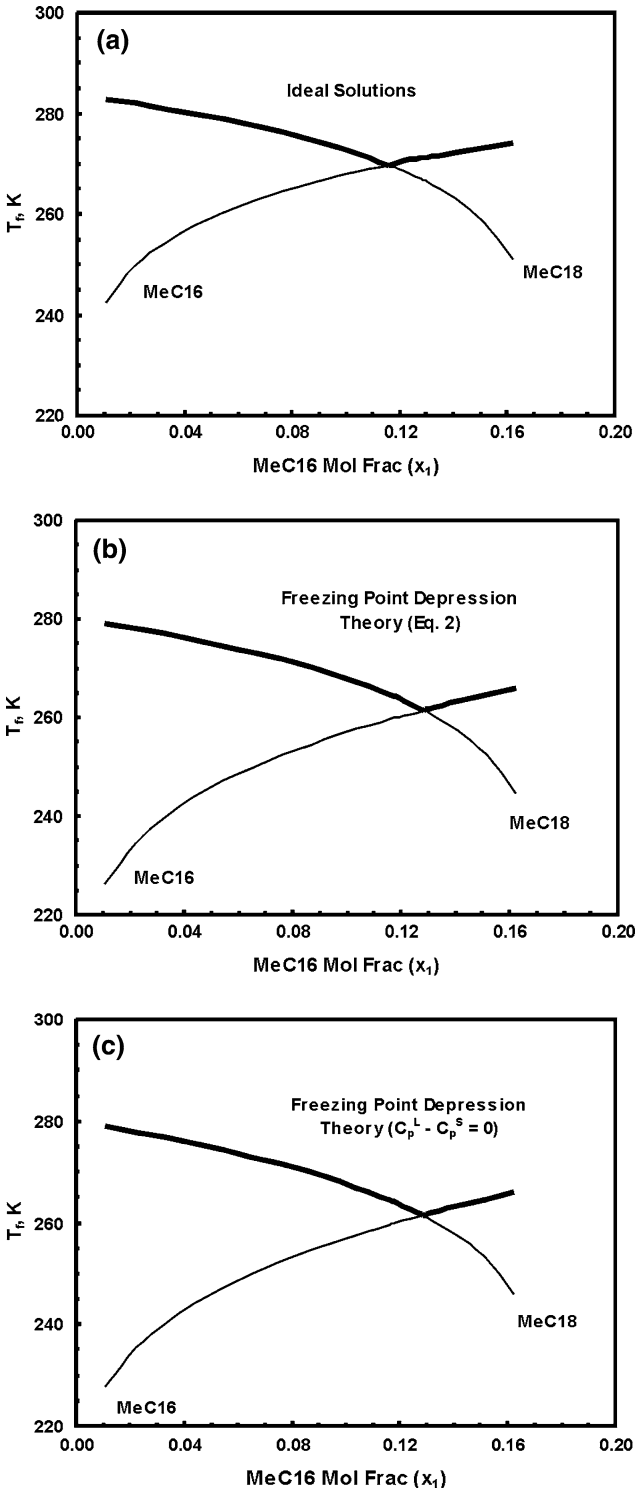

Fig. 5a–c Crystallization onset temperature (T_f) of ternary FAME mixtures (*thick lines*), as determined from calculating T_f data of MeC16 and MeC18 independently (*thin lines*). Total mass fraction of MeC16 and MeC18 $(y_1 + y_2) = 0.16$ g/g. **a** T_f values from ideal solution (Eq. 1); **b** T_f values from freezing-point depression theory (Eq. 2); **c** T_f values from Eq. 2 where $\Delta C_p = (C_p^L - C_p^S) = 0$. x_1 = mole fraction of MeC16 in ternary mixture. See Fig. 1 for other abbreviations

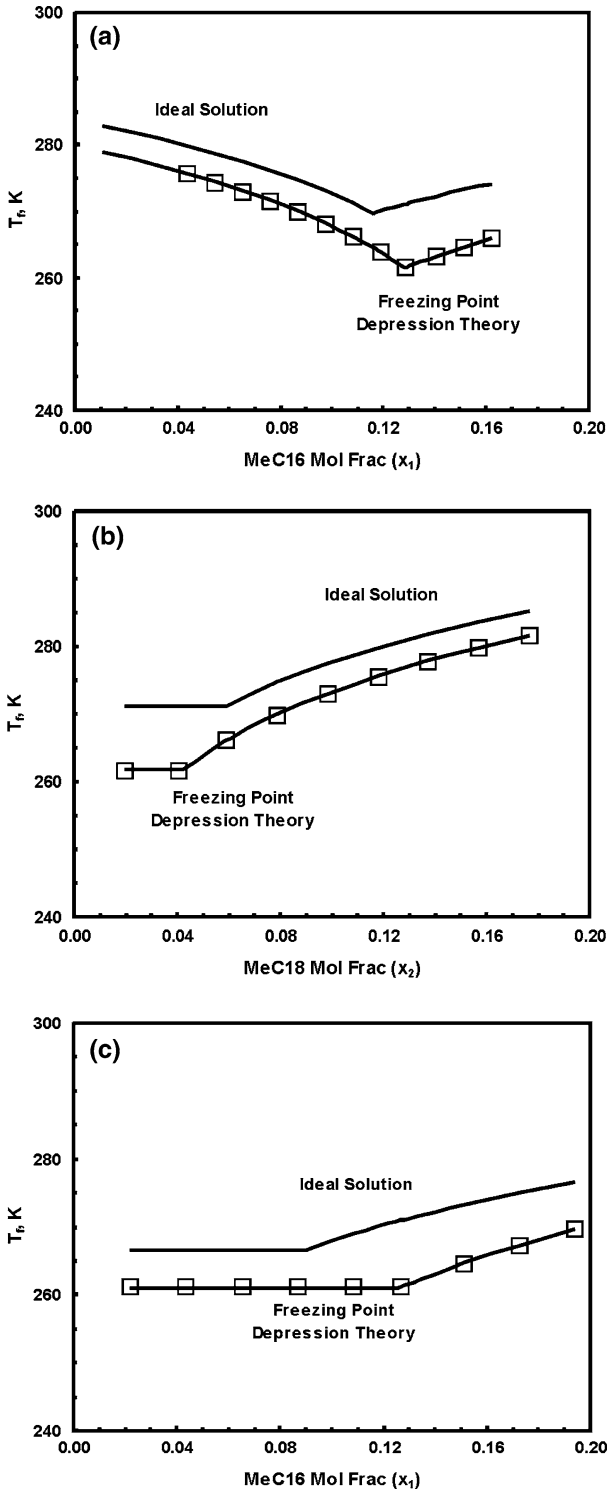

Fig. 6a–c Comparing T_f data on ternary FAME mixtures calculated from the application of ideal solution (Eq. 1), freezing-point depression theory (Eq. 2) and Eq. 2 where $\Delta C_p = 0$. **a** Constant total solute concentration $y_1 + y_2 = 0.16$ g/g in MeC18:1 solvent; **b** constant $y_1 = 0.12$ g/g MeC16 in MeC18:1 solvent; **c** constant $y_2 = 0.04$ g/g MeC18 in MeC18:1 solvent. Legend: *solid lines* (–) = T_f calculated by Eqs. 1 and 2; *squares* T_f calculated by Eq. 2 assuming $\Delta C_p = 0$. x_2 = mole fraction MeC18 in ternary mixture. See Figs. 1, 4 and 5 for other abbreviations

Table 5 Comparison of T_f data for ternary FAME mixtures of MeC16 and MeC18 in MeC18:1

y_1	y_2	x_1/x_2	T_f^{DSC}(K)	$T_f^{[1]}$(K)	$T_f^{[2]}$(K)	T_f^{H}(K)
0.02	0.14	0.16	278.4 ± 0.17	281.9	278.0	277.9
0.04	0.04	1.1	261.7 ± 0.32	266.5	261.0	261.3
0.04	0.08	0.55	268.9 ± 0.38	274.8	270.1	270.0
0.04	0.12	0.37	274.8 ± 0.19	279.9	275.8	275.6
0.04	0.12	0.37	275.8 ± 0.54	–	–	–
0.06	0.10	0.66	272.9 ± 0.55	277.6	273.2	273.0
0.08	0.04	2.2	263.6 ± 0.14	266.44	261.0	261.2
0.08	0.04	2.2	263.6 ± 0.24	–	–	–
0.08	0.08	1.1	270.3 ± 0.42	274.8	270.1	269.9
0.08	0.08	1.1	270.1 ± 0.27	–	–	–
0.09	0.04	2.5	264.5 ± 0.11	267.7	261.0	261.2
0.10	0.04	2.8	264.8 ± 0.32	268.9	261.0	261.2
0.10	0.06	1.8	268.6 ± 0.24	271.2	266.2	266.2
0.11	0.04	3.0	265.7 ± 0.45	270.1	261.0	261.4
0.12	0.01	13	263.2 ± 0.30	271.2	261.7	261.6
0.12	0.02	6.6	263.50 ± 0.062	271.24	261.73	261.63
0.12	0.03	4.4	264.7 ± 0.10	271.2	261.7	261.6
0.12	0.04	3.3	265.6 ± 0.14	271.24	261.73	261.63
0.12	0.04	3.3	266.84 ± 0.047	–	–	–
0.12	0.05	2.6	267.6 ± 0.22	271.2	264.0	263.9
0.12	0.06	2.2	269.1 ± 0.14	271.2	266.2	266.1
0.12	0.07	1.9	270.5 ± 0.30	273.0	268.1	268.0
0.12	0.08	1.7	271.6 ± 0.37	274.7	270.0	269.9
0.13	0.04	3.6	267.3 ± 0.17	272.2	263.2	263.1
0.14	0.02	7.7	265.9 ± 0.42	273.2	264.6	264.6
0.14	0.04	3.9	267.5 ± 0.24	273.2	264.6	264.6
0.15	0.04	4.1	268.48 ± 0.079	274.14	265.96	265.92
0.16	0.04	4.4	268.99 ± 0.084	275.02	267.27	267.25

Independent crystallization model results versus DSC measurements. y_1 = mass fraction of MeC16; y_2 = mass fraction of MeC18; x_1/x_2 = MeC16/MeC18 mole ratio; $T_f^{DSC} = T_f$ of ternary FAME mixture measured by DSC cooling scans at 5 °C/min; $T_f^{[1]} = T_f$ of ternary FAME mixtures calculated for an ideal solution (Eq. 1); $T_f^{[2]} = T_f$ of ternary FAME mixtures calculated from freezing-point depression theory (Eq. 2); $T_f^{H} = T_f$ of ternary FAME mixtures calculated for freezing-point depression theory assuming $(C_p^L - C_p^S) = 0$. See Tables 1, 2 and 3 for other abbreviations

The differences between the T_f results calculated for ideal solutions and the application of freezing-point depression theory were more directly compared by overlaying the resultant T_f curves from Fig. 5 in Fig. 6a. This comparison shows that lower T_f values are predicted by freezing-point depression theory than ideal solution, again an indication that the interactions between individual solute and solvent molecules in the ternary mixtures were different from the interactions between solute molecules in their pure forms. The curves in Fig. 6a also show the shift in eutectic point to a higher x_1/x_2 ratio, as noted above. At x_1 below the eutectic point, calculated T_f values for freezing point depression theory were 4–5 K below those calculated for ideal solution. Crystallization in these mixtures apparently was controlled by MeC18, which more closely resembles MeC18:1 in chemical structure than MeC16. In contrast, at x_1 above the eutectic point, crystallization was apparently controlled by MeC16, and the decreases in calculated T_f values for freezing-point depression theory increased significantly to ~9.5 K below those for ideal solution.

Data plotted in Fig. 6b and c show the effects of increasing the mass fraction (y_i) of each saturated FAME solute while holding the mass fraction of the other solute constant, where $y_1 = 0.12$ g/g in Fig. 6b and $y_2 = 0.04$ g/g in Fig. 6c. Analogous to the curves shown in Fig. 6a, curves in Fig. 6b and c demonstrate eutectic points for ideal solution and freezing-point depression theory models. Eutectic points for ideal solutions occur at ($x_2 = 0.059$; $T = 271.24$ K) in Fig. 6b and ($x_1 = 0.090$; $T = 266.44$ K) in Fig. 6c, with corresponding mole ratios (x_1/x_2) of 2.2 and 2.3. Both ratios were very close to $x_1/x_2 = 2.3$ noted above for Fig. 5a. Similarly, eutectic points for freezing point depression theory occur at ($x_2 = 0.042$; $T = 261.73$ K) in Fig. 6b and ($x_1 = 0.12$; $T = 260.96$ K) in Fig. 6c, with the corresponding $x_1/x_2 = 3.1$ and 3.2. Again, both values were very close to $x_1/x_2 = 3.1$, observed above for Fig. 5b.

Deviations between calculated mixture T_f data from ideal solution and freezing-point depression theory noted for the curves that are overlayed in Fig. 6a were also observed in Fig. 6b and c. For mixtures whose crystallization was controlled by MeC16 (that is, for compositions on the left-hand side of the eutectic in Fig. 6b or on the right hand side of the eutectic in Fig. 6c), the absolute deviations in calculated T_f were ~9.5 and 6.9–9.5 K, respectively. Analogously, for mixtures controlled by MeC18, the absolute deviations in calculated T_f were 3.5–5.4 K in Fig. 6b and ~5.4 in Fig. 6c.

Comparing the freezing-point depression theory results in Fig. 6a, b and c reveals very little deviation between the T_f values calculated explicitly from Eq. 2 and those calculated by the same equation assuming $\Delta C_p = 0$ (and $\gamma_i = \gamma_i^H$). This was shown by plotting selected data points from T_f results calculated assuming $\Delta C_p = 0$ in Fig. 6. Absolute deviations between the two applications of Eq. 2 were <0.2 K in Fig. 6a, b and <0.25 K in Fig. 6c. This demonstrates that the relative contribution of the "ΔC_p" term may be neglected in the right hand side of Eq. 2 when calculating the T_f values, under the conditions of the present study.

Comparing Calculated and Measured T_f Results

Results from direct measurement of T_f data from the analysis of DSC curves for 24 ternary FAME mixtures are

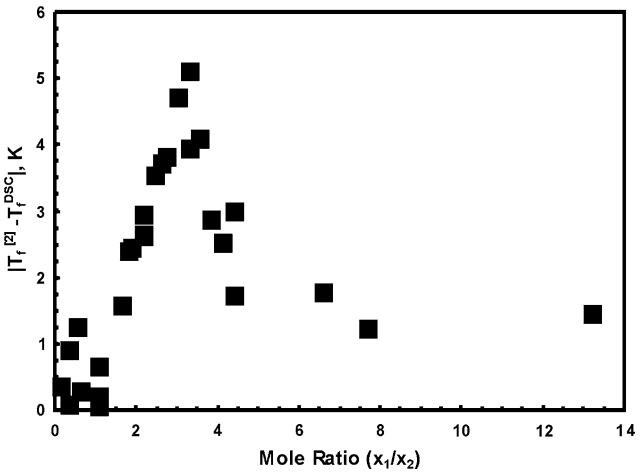

Fig. 7 Absolute value of the deviation between T_f of ternary FAME mixtures calculated by the application of freezing-point depression theory ($T_f^{[2]}$) and T_f measured by the analysis of DSC cooling curves (T_f^{DSC}). See Figs. 1 and 5 for other abbreviations

summarized under the "T_f^{DSC}" heading in Table 5. Alongside those results are corresponding values predicted for the ideal solution and freezing-point depression theory models: '$T_f^{[1]}$" by Eq. 1; "$T_f^{[2]}$" by Eq. 2; and "T_f^{H}" by Eq. 2 and assuming $\Delta C_p = 0$.

Absolute values of the deviation between $T_f^{[2]}$ and T_f^{DSC} ($\Delta T_f = |T_f^{[2]} - T_f^{DSC}|$) were plotted as a function of x_1/x_2 mole ratio in Fig. 7. The resulting δT_f values were within the range 0.1–5.11 K with a mean value = 2.2 K. A similar comparison between $T_f^{[1]}$ for ideal solutions and T_f^{DSC} yielded absolute deviations in the range 2.1–8.1 K with a mean value = 4.7 K. Overall, it was more accurate to calculate T_f from the application of freezing-point depression theory than ideal solution.

Ternary mixtures demonstrating the largest δT_f values in Fig. 7 were oriented about x_1/x_2 mole ratio = 3.3. This mole ratio is very close to the eutectic point at $x_1/x_2 = 3.2$ predicted by the application of freezing-point depression theory, as discussed above. On the other hand, δT_f values were minimized for $x_1/x_2 < 1.7$ or $x_1/x_2 > 6.6$. In several cases, δT_f values were within the SD of T_f^{DSC}. These observations suggest that the crystallization behavior of ternary FAME mixtures at low temperatures may be controlled by one or the other solute species, depending on their mole ratio. At low ratios, MeC18 is the dominant solute species, while at higher ratios MeC16 dictates the onset of crystallization. Mixtures with solute ratios near the eutectic point appear to reside in a transition region where both MeC16 and MeC18 may influence crystallization, leading to higher deviations between T_f data calculated from the application of freezing-point depression theory and that from analysis by DSC.

In conclusion, the present study shows that crystallization behavior in FAME mixtures may be predicted if accurate data for composition (x_i), ΔH_{fus} and MP are available. This should be valid for more complex mixtures of FAME than those studied herein. Although ideal solution generally predicts T_f values that are higher than for nonideal mixtures, the application of Eq. 1 may be appropriate for estimating the crystallization onset temperature within 5 °C. In cases where γ_i data are available for specific solute–solvent compositions, Eq. 2 may be employed, neglecting the ΔC_p term, in order to obtain more accurate crystallization onset temperatures.

Acknowledgments Technical assistance on this project was provided by K. Ascherl, H. Khoury, R. Sanders and K. Steidley. In addition, G. Suppes and R. Fillieres provided consultation on the development of experimental studies and the interpretation of results.

References

1. Knothe G, Dunn RO (2005) Biodiesel: an alternative diesel fuel from vegetable oils or animal fats. In: Erhan SZ (ed) Industrial uses of vegetable oils. AOCS, Champaign, IL, pp 42–89
2. Knothe G, Dunn RO (2001) Biofuels derived from vegetable oils and fats. In: Gunstone FD, Hamilton RJ (eds) Oleochemical manufacture and applications. Sheffield Academic, Sheffield, UK, pp 106–163
3. Graboski MS, McCormick RL (1998) Combustion of fat and vegetable oil derived fuels in diesel engines. Prog Energy Combust Sci 24:125–164
4. Schwab AW, Bagby MO, Freedman B (1987) Preparation and properties of diesel fuels from vegetable oils. Fuel 66:1373–1378
5. Van Gerpen JH, Soylu S, Tat ME (1999) Evaluation of the lubricity of soybean oil-based additives in diesel fuels (Paper No. 996314). In: Proceedings of the Annual Meeting of the ASAE, Toronto, ON, Canada, 18–21 July 1999. American Society of Agricultural Engineers, St. Joseph, MI
6. Sheehan J, Camobreco V, Duffield J, Graboski M, Shapouri H (1998) Life cycle inventory of biodiesel and petroleum diesel for use in an urban bus (Final Report No. NREL-SR–580–24089). National Renewable Energy Laboratory, Golden, CO, pp 206–261
7. USEPA (2002) A comprehensive analysis of biodiesel impacts on exhaust emissions (Draft Technical Report No. EPA420-P-02-001). US Environmental Protection Agency, Washington, DC
8. Dunn RO (2005) Cold weather properties and performance of biodiesel. In: Knothe G, Krahl J, Van Gerpen J (eds) The biodiesel handbook. AOCS Press, Champaign, IL, p 83
9. Cold Flow Consortium Committee (2005) Evaluation of temperature effects for blending biodiesel at 2% with #1 kerosene and #2 diesel (National Cold Weather Blending Study). National Biodiesel Board, Jefferson City, MO, pp 5–6 (see http://www.biodiesel.org/resources/reportsdatabase/reports/gen/20050728_Gen-354.pdf, last accessed 24 July 2008)
10. Fukuda H, Koda A, Noda H (2001) Biodiesel fuel production by transesterification of oils. J Biosci Bioeng 92:405–416
11. Foglia TA, Nelson LA, Dunn RO, Marmer WN (1997) Low-temperature properties of alkyl esters of tallow and grease. J Am Oil Chem Soc 74:951–955
12. Masjuki H, Zaki AM, Sapuan SM (1993) Methyl ester of palm oil as an alternative diesel Fuel. In: Proceedings of the 2nd Institute

of Mechanical Engineers Seminar: Fuels for Automotive and Industrial Diesel Engines. Institute of Mechanical Engineers, London, pp 129–137
13. González-Gómez ME, Howard-Hildige R, Leahy JJ, Rice B (2002) Winterization of waste cooking oil methyl ester to improve cold flow temperature fuel properties. Fuel 81:33–39
14. Dunn RO, Shockley MW, Bagby MO (1997) Winterized methyl esters from soybean oil: an alternative diesel fuel with improved low-temperature flow properties (Paper No. 971682). In: State of alternative fuel technologies (SAE Spec Publ SP-1274). Society of Automotive Engineers, Warrendale, PA, pp 133–142
15. Dunn RO, Shockley MW, Bagby MO (1996) Improving the low-temperature flow properties of alternative diesel fuels: vegetable oil-derived methyl esters. J Am Oil Chem Soc 73:1719–1728
16. Lee I, Johnson LA, Hammond EG (1996) Reducing the crystallization temperature of biodiesel by winterizing methyl soyate. J Am Oil Chem Soc 73:631–636
17. Lide DR (1990) CRC handbook of chemistry and physics, 71st edn. CRC Press, Boca Raton, FL, pp 3355–3465
18. Dean JA (1999) Lange's handbook of chemistry, 15th edn. McGraw-Hill, New York, pp 1268–1274
19. Dunn RO (1998) Effect of winterization on fuel properties of methyl soyate. In: Peterson CL (ed) Commercialization of Biodiesel: Producing a Quality Fuel (Conference Proceedings). University of Idaho, Moscow, ID, pp 164–186
20. Holder GA, Winkler J (1965) Wax crystallization from diesel fuels. J Inst Pet 51:228–252
21. Toro-Vazquez JF, Briceño-Montelongo M, Dibildox-Alvarado E, Charó-Alonso M, Reyes-Hernández J (2000) Crystallization kinetics of palm stearin in blends with sesame seed oil. J Am Oil Chem Soc 77:297–310
22. Suppes GJ, Fox TJ, Gerdes KR, Jin H, Burkhard ML, Koert DN (2000) Cold flow and ignition properties of Fischer–Tropsch fuels (SAE Tech Paper Series No. 2000-01-2014). Society of Automotive Engineers, Warrendale, PA
23. Imahara H, Minami E, Saka S (2006) Thermodynamic study on cloud point of biodiesel with its fatty acid composition. Fuel 85:1666–1670
24. Rodrigues Jr J de A, Cardoso F de P, Lachter ER, Estevão LRM, Nascimento RSV (2006) Correlating chemical structure and physical properties of vegetable oil esters. J Am Oil Chem Soc 83:353–357
25. Bailey AE (1950) Melting and solidification of fats. Interscience, New York, p 172